

Microphysical and Dynamical Characteristics of Low-Precipitation and Classic Supercells

LEAH D. GRANT AND SUSAN C. VAN DEN HEEVER

Colorado State University, Fort Collins, Colorado

(Manuscript received 21 August 2013, in final form 3 March 2014)

ABSTRACT

The sensitivity of supercell morphology to the vertical distribution of moisture is investigated in this study using a cloud-resolving model with 300-m horizontal grid spacing. Simulated storms are found to transition from classic (CL) to low-precipitation (LP) supercells when the strength of elevated dry layers in the environmental moisture profile is increased. Resulting differences in the microphysical and dynamical characteristics of the CL and LPs are analyzed.

The LPs produce approximately half of the accumulated surface precipitation as the CL supercell. The precipitating area in the LPs is spatially smaller and overall less intense, especially in the rear-flank downdraft region. The LPs have smaller deviant rightward storm motion compared to the CL supercell, and updrafts are narrower and more tilted, in agreement with observations. Lower relative humidities within the dry layers enhance evaporation and erode the upshear cloud edge in the LPs. This combination favors a downshear distribution of hydrometeors. As a result, hail grows preferentially along the northeastern side of the updraft in the LPs as hail embryos are advected cyclonically around the mesocyclone, whereas the primary midlevel hail growth mechanism in the CL supercell follows the classic Browning and Foote model. The differing dominant hail growth mechanisms can explain the variations in surface precipitation distribution between CLs and LPs. While large changes in the microphysical structure are seen, similarities in the structure and strength of the updraft and vorticity indicate that LP and CL supercells are not dynamically distinct storm types.

1. Introduction

The supercell storm spectrum represents a continuum of supercell types that are commonly divided into three main classes: low-precipitation (LP), classic (CL), and high-precipitation (HP) supercells. LPs have strong and long-lived rotating updrafts, as do all supercells, but their precipitation rates are comparatively weaker. They are low-precipitation-efficiency storms even amongst supercells, which themselves are a low-precipitation-efficiency storm class (Browning 1977).

More intense precipitation is typically located within the forward-flank downdraft (FFD) region in LPs, while the rear-flank downdraft (RFD) and updraft core usually contain only a few large hydrometeors (Bluestein and Parks 1983, hereafter BP83; Bluestein 1984). Additionally, observations of LPs report narrow updrafts often located to the rear of the main radar echo that may be

tilted or upright, hail and large raindrops falling from the anvil, and a lack of strong cold pools (Davies-Jones et al. 1976; Burgess and Davies-Jones 1979, hereafter BD79; BP83; Bluestein 1984; Bluestein and Woodall 1990; Moller et al. 1994). Observations of significant overshooting tops (e.g., up to 4 km above the equilibrium level reported in BD79) indicate that LP supercells are not simply weaker versions of their classic counterparts. Though LPs are often isolated, they sometimes occur in relatively close proximity to CL supercells or other convection; in these cases, the LP is typically the farthest upwind of the storms (BP83; Rasmussen and Straka 1998, hereafter RS98). LPs form most frequently in the high plains of the United States and along the dryline (BD79; Moller et al. 1994).

The mechanisms that distinguish LPs from CL supercells are not well understood, though a number of hypotheses have been put forward. Brooks et al. (1994) suggest that the strength of the low- and midlevel wind shear can affect which supercell archetype forms through its impacts on the strength of the mesocyclone, storm-relative winds, and advection of hydrometeors within

Corresponding author address: Leah D. Grant, Colorado State University, 1371 Campus Delivery, Fort Collins, CO 80523.
E-mail: ldgrant@atmos.colostate.edu

the storm. RS98 hypothesize, based on environmental sounding data, that upper-level storm-relative winds and upper-level humidity are potential discriminators. BD79 first noted the connection between LPs and the dryline, highlighting the potential importance of low-level moisture; BP83 also found that LPs form in environments that are drier (all the LP storms in their study occurred near the dryline). Drop size spectra, through their impact on collision-coalescence processes (Weisman and Bluestein 1985; Bluestein and Woodall 1990) and the size of the initial convective element (BP83; Brooks and Wilhelmson 1992) have also been suggested as storm morphology discriminators.

Environmental factors leading to LP supercells are not well understood because 1) observations of LP supercells are limited owing to the subjectivity of their classification and difficulty to detect with radar; 2) LP and CL supercells sometimes occur in close proximity to one another, and therefore the environmental humidity and vertical shear profiles may vary on scales not measurable by the rawinsonde network; and 3) high-resolution simulations with sophisticated microphysics have not yet been performed (Beatty et al. 2008). In one modeling study, an LP-like storm was simulated by artificially shutting off rain formation in the model and forcing all condensed water to remain as cloud water (Weisman and Bluestein 1985). In another study, Brooks and Wilhelmson (1992) used a smaller warm bubble for storm initialization and likened the resulting storm precipitation characteristics to an LP supercell. However, the simulated LP storm contained weak updrafts of less than 10 m s^{-1} .

Though it is not known which factor(s) lead to LP supercells, the environments in which they typically form are often characterized by elevated layers of lower relative humidity that can vary in both strength and altitude. The goal of the research presented here is therefore twofold: 1) to investigate the sensitivity of supercell storm morphology to changes in the vertical moisture profile and the physical processes by which these varying moisture profiles impact supercellular storm structure, and 2) to assess whether differences in the dynamical and microphysical characteristics of these storm types do exist and hence produce their differing precipitation distributions.

To address these goals, idealized simulations of supercell storms were performed with a cloud-resolving model. A CL supercell was first simulated. Next, because dry layers are common in environments where LPs occur, the environmental moisture profile was systematically altered by adding dry layers of varying magnitudes and altitudes. It will be shown in this study that LP supercells form when more elevated dry layers are present in the environmental profile. The microphysical structure and

dominant hail growth mechanisms are found to differ in LPs compared to CL supercells. The broad dynamical structure, however, is found to be similar among the different storm types.

The organization of this paper is as follows: Section 2 describes the model used and the design of the sensitivity experiments. Section 3 presents (i) an overview of the simulation evolutions and supercell precipitation characteristics, (ii) a comparison of the simulated supercell structure and dynamical features, and (iii) an analysis of microphysical fields and budgets. Different hail growth mechanisms in the CL and LPs are presented in section 4. In section 5, previous hypotheses regarding supercell morphology, future work, and potential applications for forecasting are discussed. A summary is provided in section 6.

2. Model setup and experiment design

The Regional Atmospheric Modeling System (RAMS), version 6, was used to achieve the goals of this study (Cotton et al. 2003; Saleeby and van den Heever 2013). RAMS is a nonhydrostatic, regional model appropriate for simulating a wide range of scales of atmospheric phenomena. For these experiments, RAMS was set up as a cloud-resolving model with 300-m horizontal grid spacing and a single grid with a domain size of $285 \text{ km} \times 225 \text{ km}$. The vertical grid spacing was 25 m at the surface and was vertically stretched to a maximum of 300 m. The domain top was located approximately 22 km AGL (hereafter, all heights are AGL). There were 92 vertical levels, 17 of which were below 1 km. The time step was 1 s, and experiments were run for 3 simulation hours. The model configuration is detailed in Table 1.

RAMS uses a sophisticated two-moment bulk microphysics scheme that prognoses mass and number concentration for eight hydrometeor classes: cloud, drizzle, rain, pristine ice, snow, aggregates, graupel, and hail. RAMS also utilizes bin-emulating procedures for cloud droplet nucleation, riming, and sedimentation. The microphysics code tracks detailed microphysical budgets, which is crucial for microphysical process studies. Further details on various aspects of the RAMS microphysics scheme may be found in Walko et al. (1995), Meyers et al. (1997), Saleeby and Cotton (2004, 2008), and Saleeby and van den Heever (2013).

The model domain was initialized with vertically varying but horizontally homogeneous conditions. The control (CTL) experiment thermodynamic profile follows the analytical profile of Weisman and Klemp (1982) with a vapor mixing ratio of 13 g kg^{-1} in the well-mixed boundary layer. The initial CTL temperature and dewpoint profiles are shown in blue in Fig. 1a. Surface-based

TABLE 1. RAMS configuration and options chosen for the simulations described in the text.

Model aspect	Setting
Grid	Arakawa C grid $\Delta x = \Delta y = 300$ m; 950×750 points $\Delta z =$ variable Minimum $\Delta z = 25$ m, maximum $\Delta z = 300$ m Vertical stretch ratio = 1.1 92 total vertical levels; 17 levels below 1 km AGL Model top ≈ 22 km
Time step	1 s
Simulation duration	3 h
Initialization	Horizontally homogeneous thermodynamic and wind shear profile
Convective initialization	2-K thermal perturbation 10 km \times 10 km bubble 3-km depth
Boundary conditions	Radiative lateral boundary (Klemp and Wilhelmson 1978) Rayleigh friction damping over top six vertical levels (~ 20 – 22 km AGL) No surface fluxes
Microphysics scheme	Two-moment bulk microphysics (Meyers et al. 1997) Eight hydrometeor classes (Saleeby and Cotton 2004)
Aerosol treatment	Two aerosol species: sulfates and dust (Saleeby and van den Heever 2013) Linearly decreasing sulfate and dust concentration profile from 100 cm^{-3} at the surface to 10 cm^{-3} at 4 km AGL; constant thereafter No aerosol sources or sinks DeMott et al. (2010) ice nucleation parameterization
Turbulence scheme	Smagorinsky (1963) deformation- K with stability modifications by Lilly (1962) and Hill (1974)
Radiation scheme	None
Coriolis	No

convective available potential energy (CAPE) in this environment approaches 1800 J kg^{-1} .

An idealized half-circle shear profile was used in which wind speeds increased from 0 m s^{-1} at the surface to 32 m s^{-1} at 5 km AGL, following the strongest shear case tested in Weisman and Klemp (1984) (Fig. 1b). Wind speeds increased slowly to 34 m s^{-1} by 7 km AGL, with no further vertical wind shear above 7 km. This shear and instability combination is conducive for supercell development, and the clockwise-turning hodograph favors the right-moving storms (Weisman and Klemp 1984). The idealized half-circle hodograph shape has been used extensively in modeling studies of supercells (e.g., Weisman and Klemp 1984; Droegemeier et al. 1993; McCaul and Cohen 2002), and the magnitude of the shear is representative of previously observed LP supercell environments [e.g., BD79, their Fig. 2; Bluestein and Woodall (1990), their Fig. 7; MacGorman and Burgess (1994), their Table 1 for the 26 March 1991 case].

To address the goals of this study, nine additional sensitivity simulations were designed with varying environmental moisture profiles. Moisture mass was systematically reduced from the CTL vapor mixing ratio profile within a 1-km-deep layer; these layers will simply be referred to as dry layers. The various imposed dry layers were located at three different heights: 1.5–2.5, 2–3, and

3–4 km. Such dry layers often occur above the well-mixed boundary layer near the dryline or in the high plains owing to the elevated mixed layer, such as shown in Ziegler and Rasmussen (1998, their Fig. 3), Cai et al. (2006, their Fig. 18), and Parker (2012, his Fig. 1). The vapor mixing ratio was linearly interpolated to the original profile at 1 km below and 2 km above the dry layer, and the final profile was then smoothed. The addition of various dry layers—one for each experiment—is also depicted in Fig. 1a. Throughout the rest of the paper, these experiments will be referenced using a letter and number, where the first letter is either L (low), M (middle), or H (high), referring to the height of the dry layer, and the number is either 25, 50, or 75, referring to the vapor mixing ratio reduction percentage. For example, H75 refers to the experiment with the strongest (75%) reduction in mixing ratio within the highest vertical layer. The experiment names and dry layer setups are summarized in Table 2. The precipitable water (PW) for each simulation, which varies from approximately 30 to 45 mm, and the percentage change from CTL are listed in Table 3.

In the interest of performing a controlled experiment, the moisture profile was kept identical in each simulation except within the imposed dry layer. In this way, the surface-based and most unstable CAPE, rather than the

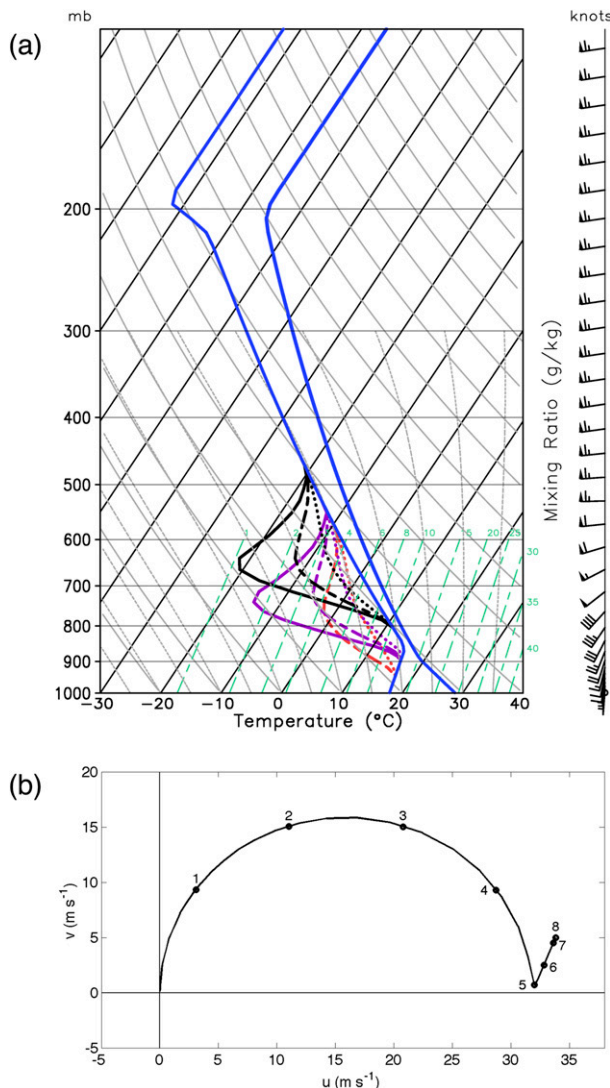


FIG. 1. (a) Initial thermodynamic temperature and dewpoint profile used for the CTL experiment (blue lines), following Weisman and Klemp (1982), and the initial wind profile used for all simulations (barbs, kt). Dewpoint profiles for the various dry layer sensitivity experiments as described in the text are also shown. Black: highest dry layer (H); purple: middle dry layer (M); red: lowest dry layer (L); dotted: 25% moisture reduction; long-short dashed: 50% moisture reduction; solid: 75% moisture reduction. (b) Hodograph of the initial winds used for all simulations, following Weisman and Klemp (1984). Labeled points are kilometers AGL.

mixed-layer CAPE, are kept constant for each case, save for small variations (<5%) due to the virtual temperature effect. Note that the lowest and middle dry layers deplete moisture from the well-mixed layer. This reduces the mixed-layer CAPE by about 10% and 20% in L25 and L50, respectively, but it does not change the mixed-layer CAPE by more than a few percent in M25–75. Consequently, M was the lowest dry layer that

TABLE 2. Sensitivity experiment nomenclature and the imposed dry-layer characteristics. Note that L75 was not performed and hence is not listed in the table.

Dry-layer characteristic	Vapor mixing ratio reduction		
	75%	50%	25%
Highest (center 3.5 km AGL)	H75	H50	H25
Middle (center 2.5 km AGL)	M75	M50	M25
Lowest (center 2.0 km AGL)	—	L50	L25

supported sustained convection. Simulation L75 was therefore not performed, and simulations L25 and L50 will only be briefly discussed in section 3a below.

While the observed example dryline and high plains soundings referenced earlier contain dry air confined within a layer, it is perhaps more common for dry air aloft to extend upward throughout the troposphere. Furthermore, as stated in Weisman and Klemp (1982), the analytical sounding is too moist in the upper levels compared to soundings representative of midlatitude severe weather situations. Two sensitivity experiments were therefore performed in which the vapor mixing ratio was reduced by 50% above 6 km for experiments CTL and H50 (not shown). Very little change in the simulation evolutions, accumulated precipitation, and storm structure were found. Therefore, the results presented in this study do not appear to depend on the presence of the overlying moist layer above the imposed dry layer.

3. Results

a. Simulation evolution and precipitation characteristics

General characteristics of each simulation evolution are evident in the accumulated surface precipitation field (Fig. 2). First, given the imposed veering wind profile, the initial thermal in CTL evolves into a convective storm that splits into a right mover (RM)—which becomes the

TABLE 3. Precipitable water (PW) for each simulation performed and the percentage change in PW from CTL.

Simulation name	PW (mm)	Change in PW from CTL (%)
CTL	44.05	—
L25	38.64	−12.3
L50	33.16	−24.7
M25	39.70	−9.9
M50	35.34	−19.8
M75	30.97	−29.7
H25	41.46	−5.9
H50	38.86	−11.8
H75	36.25	−17.7

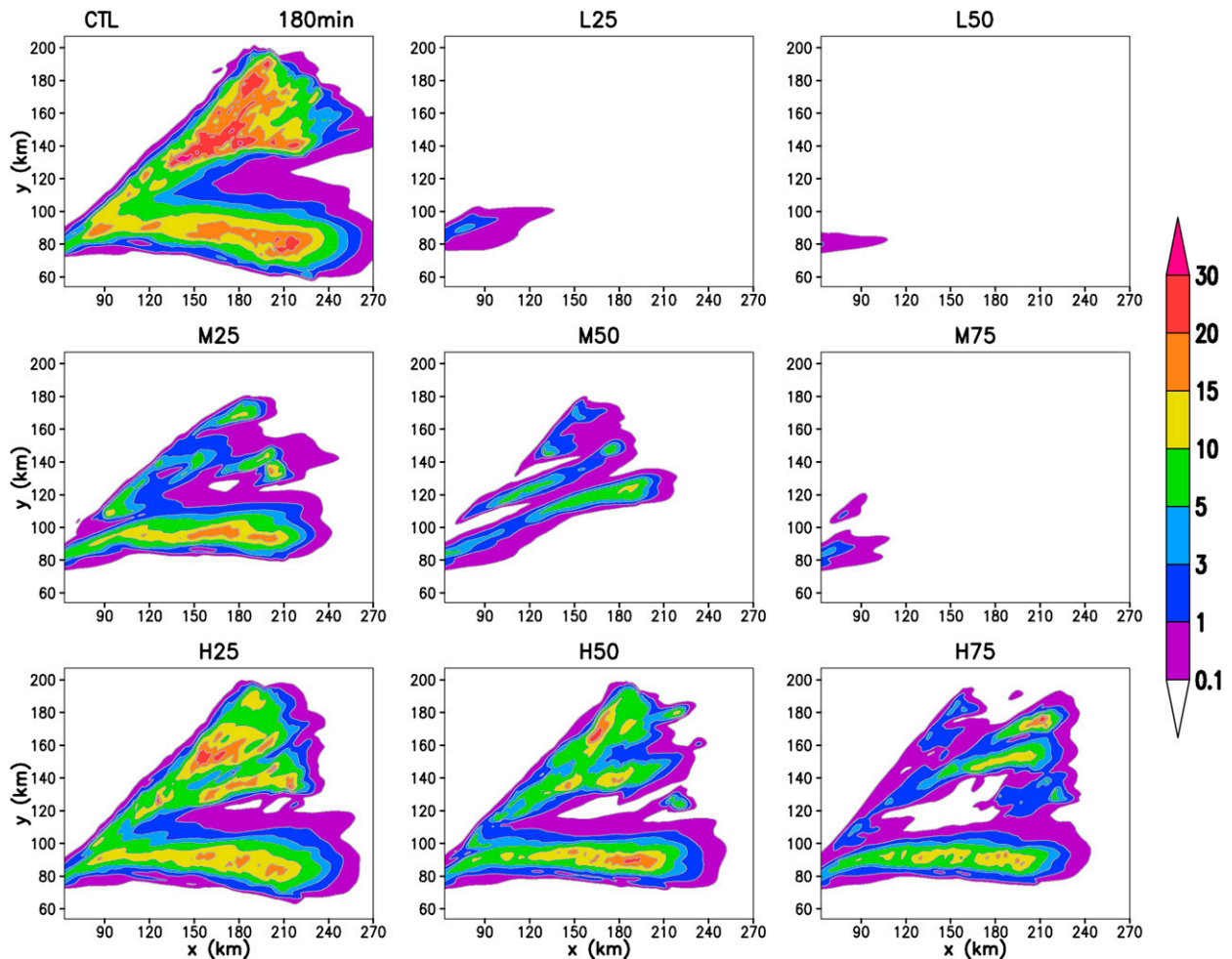


FIG. 2. Total accumulated surface precipitation (mm, shaded) after three simulation hours for (top) CTL, L25, and L50, and all (middle) M and (bottom) H sensitivity experiments.

dominant, relatively steady supercell—and a left mover (LM), which later undergoes additional storm splitting. In CTL, splitting is first evident in the midlevel updraft after 45 min.

The initial storm split and the same general precipitation pattern are evident in experiments CTL, M25, H25, H50, and H75, although it can be seen by comparing these five experiments that the RM in CTL takes a sharper right turn than in the other experiments. This is broadly consistent with *BD79*'s observations of tornado-producing LP supercells that did not have significant right-turning motion, unlike previously observed CL supercells at that time. *BP83* also found that LPs move less to the right of the mean wind shear than CL supercells, although it was noted that this result was significant at slightly below the 95% confidence level.

It is clear that the highest accumulated surface precipitation occurs in CTL compared to all of the dry-layer

experiments. Accumulated precipitation for the CTL RM reaches a maximum of 26.8 mm at the end of the simulation, whereas it only once exceeds 20 mm in H50 and not at all in the other simulations. Domainwide accumulated precipitation is reduced as the dry layer strength is increased, especially in the precipitation resulting from the initial LM.

The environments in M75 and all the experiments with the lowest dry layer are not supportive of sustained convection. The initial convection quickly dissipates in these scenarios; maximum accumulated precipitation is less than 4.5 mm in each. The simulation evolution in M50 is also substantially different. In M50, the initial RM takes much longer to become organized, and its path is therefore displaced farther north. Since moisture was depleted from the top of the mixed layer in the M and L experiments, these results are consistent with those in *BP83*. They found that the moist-layer depth did not differ

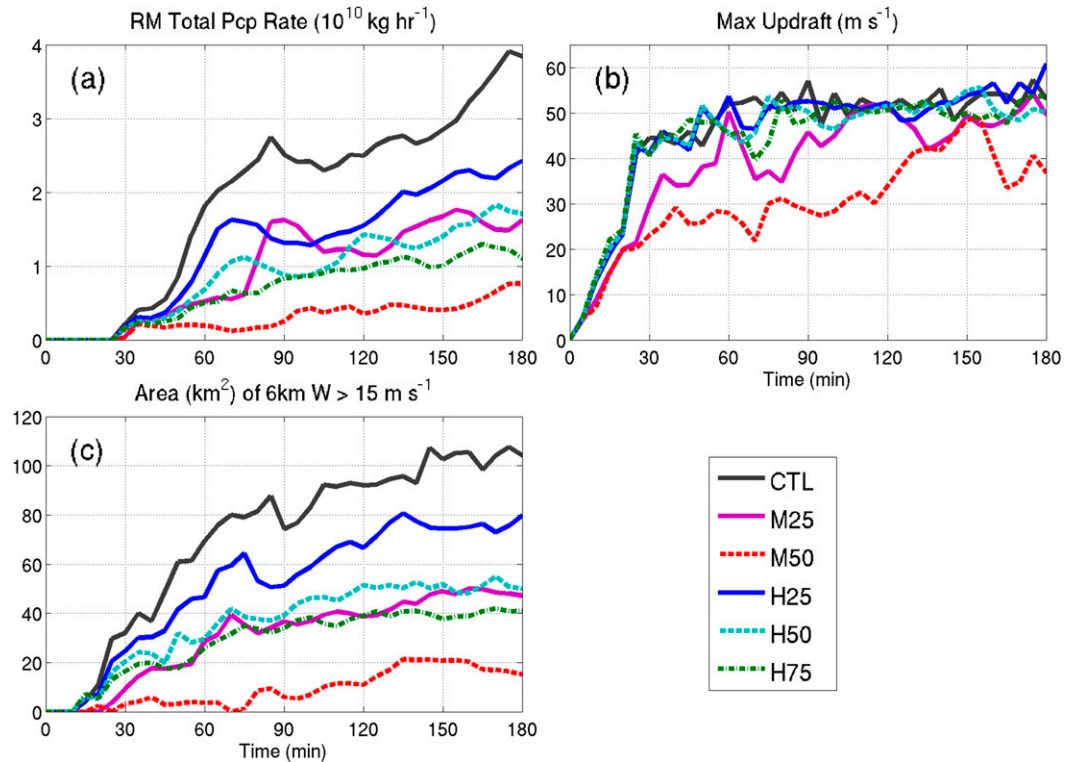


FIG. 3. (a) Time series of the total surface precipitation rate ($10^{10} \text{ kg h}^{-1}$) for the RM storm in simulations CTL, M25, M50, and all H sensitivity experiments. Total precipitation rate is calculated from the accumulated surface precipitation field using the formula discussed in the text. (b) Time series of the domain-maximum updraft speed (m s^{-1}) for each RM. (c) Time series of the area of the RM updraft (km^2) where vertical velocity exceeds 15 m s^{-1} at approximately 6 km AGL.

between CL and LP environments. Additionally, McCaul and Cohen (2002) showed that simulated supercells were more intense under more CAPE-starved environments when the mixed-layer and moist-layer depths were increased.

The weakest dry layer has much more of an impact on accumulated surface precipitation when placed at mid-levels (M25) compared with higher levels (H25), though the spatial pattern is similar between the two. In fact, total precipitation in H25 is the most similar to CTL. Furthermore, accumulated precipitation is higher in simulation H50 than in M25, although the reduction in PW is slightly greater for H50 (Table 3). Thus, simulated storm precipitation characteristics and, as will be shown, updraft steadiness and strength (Fig. 3b) are significantly more sensitive to the imposed dry layer when it depletes moisture from the well-mixed boundary layer (M and L experiments) than when it does not (H experiments), again in agreement with McCaul and Cohen (2002) and BP83.

Since one objective of this study is to compare the microphysical and dynamical processes within CL and LP supercells, the analysis will focus on the RM storm for the

rest of this paper. Only six experiments produced an RM supercell. The total precipitation rate over the RM track, shown in Fig. 3a, is calculated as the rate of change of accumulated surface precipitation (kg s^{-1}) by the formula $\Delta[(\sum_{dA} \text{accumulated_precip} > 1 \text{ mm}) dx dy]/\Delta t$. This takes into account the intensity of the RM precipitation, as well as its spatial extent. Experiment CTL produces the most precipitation. The total RM surface precipitation is systematically reduced as the dry-layer strength increases and as the dry-layer altitude decreases, in agreement with the results shown in Fig. 2. There is some indication that a limit exists on the extent to which the dry layer can impact the precipitation; for example, the reduction in the RM precipitation rate between CTL and H25 is larger than the reduction between H25 and H50, and the change in precipitation rate between H50 and H75 is relatively small.

The reduced RM surface precipitation rate in the various dry-layer experiments does not occur because the dry layer reduces the storm's updraft strength, except perhaps in M50 and at times in M25 (Fig. 3b). The CTL and all the highest dry layer experiments exhibit similar maximum updraft speeds around 50 m s^{-1} once

they reach a relatively steady state, particularly after about 90 simulation minutes. The RM supercells in M25 and M50 are more unsteady in comparison. Maximum updraft strength varies by 10–15 m s^{-1} in M25, although it does occasionally exceed 50 m s^{-1} . The M50 RM is a weaker storm overall; its maximum updraft strength exceeds 40 m s^{-1} for only about 30 min.

Though updraft strength is comparable among the supercells, especially between CTL and H25–75, the dry-layer RM supercells have narrower updrafts (Fig. 3c). The area of updraft exceeding 15 m s^{-1} at 6 km in CTL is about twice as large as the updraft area in M25, H50, and H75. This is consistent with observations of LP supercells resembling “skeletons” of CL supercells with narrower updrafts (BP83).

The rest of this analysis will focus on the CTL, M25, H50, and H75 RM supercells. These four are chosen because M25, H50, and H75 have similar updraft and precipitation characteristics and resemble LP supercells, as is seen in Fig. 3 and will be discussed in further detail in the following subsections. M50 is excluded because it is a weaker storm. H25 cannot easily be defined as an LP supercell, as it has an updraft area and precipitation characteristics between that of the CTL RM and the other dry-layer RMs (Figs. 3a and 3c).

Temporal evolution of surface precipitation rate, and maximum updrafts and downdrafts within the lowest 1 km, for the last 20 simulation minutes are depicted in Fig. 4 for the above-mentioned four RM supercells. The CTL RM exhibits characteristics of CL supercell storms. The FFD region contains heavy precipitation. In the RFD region to the west of the main low-level updraft, precipitation rates typically reach 60–75 mm h^{-1} throughout the last 30 simulation minutes and even exceed 100 mm h^{-1} at 150 min (not shown). The precipitation field clearly resembles the typical hook-echo structure of CL supercells.

Though the RMs in dry-layer experiments M25, H50, and H75 also exhibit these general RFD and FFD precipitation features, the RFD precipitation is less intense, particularly in H50 and H75 (Fig. 4, from approximately $x = -5$ to $x = -2$ and $y = 0$ in each panel). Specifically, RFD precipitation rates are typically about 30–60 mm h^{-1} in M25, 15–30 mm h^{-1} in H50, and 15–45 mm h^{-1} in H75 compared to 60–75 mm h^{-1} in CTL. The RFD also covers a smaller area. It is separated from the region of FFD precipitation by lighter precipitation rates in comparison with CTL, where the FFD and RFD precipitation are more continuously connected.

The spatial distribution of the FFD precipitation is notably different in the dry-layer supercells compared with CTL. H50 and H75 have an elongated region of light precipitation extending downwind (with respect to

the upper-level winds) of the heaviest FFD precipitation, and the north–south extent of this precipitation is reduced, particularly in H75, when compared to CTL. The FFD precipitation in M25 is not as elongated as in H50 and H75; rather, the M25 supercell looks more like a spatially smaller and less intense version of CTL with a less-well-defined RFD.

To summarize, when elevated or weak dry layers are present in the moisture profile (M25, H50, and H75), strong RM storms form that have characteristics of LP supercells. These features include narrower updrafts, reduced surface precipitation rates, and a different RFD and FFD precipitation spatial pattern than in a CL supercell. In the next section, storm structure and dynamical characteristics of the CTL, M25, H50, and H75 supercells are compared and related to the differences noted in the precipitation features. The rest of the analysis will focus on the last 20 simulation minutes when the updraft strengths are similar among the four supercells (Fig. 3b).

b. Storm structure and dynamical features

The broad dynamical structure of the CTL, M25, H50, and H75 RM supercells is demonstrated in Fig. 5. Since the imposed environmental wind profile is strongly veering, each RM supercell ingests streamwise vorticity into its updraft owing to its deviant rightward motion off the hodograph. The resultant mesocyclone structure is fairly similar among the supercells. A deep column of rotation exists within each updraft, and vertical relative vorticity exceeding 0.01 s^{-1} extends from at least 3 km up through 10 km, meeting the commonly accepted definition of a supercell storm (e.g., Doswell and Burgess 1993).

At the time shown in Fig. 5 (180 min), moderate updraft speeds (10 and 25 m s^{-1} contours) extend higher into the storm in the CTL and H75 supercells than in the other two. However, the updraft heights vary considerably with time for each storm because of fluctuations in updraft strength resulting from low-level convergence and hydrometeor loading. The updraft is narrower in the dry-layer supercells, as first shown in Fig. 3c, which is a consistent feature throughout the analysis time.

The broad updraft region is circular in the CTL supercell (Fig. 6), while updraft speeds greater than 25 m s^{-1} take on a typical horseshoe shape (e.g., Lemon and Doswell 1979; Byko et al. 2009). The dry-layer supercell updraft shapes look similar to CTL, but they are more elongated along the northwest–southeast direction. In CTL, a region of updraft speeds between 10 and 25 m s^{-1} is located in the west-northwest portion of the updraft. Enclosed in this region is a spatially small and strong positive and negative couplet of vorticity, with the negative vorticity located about 3 km to the east

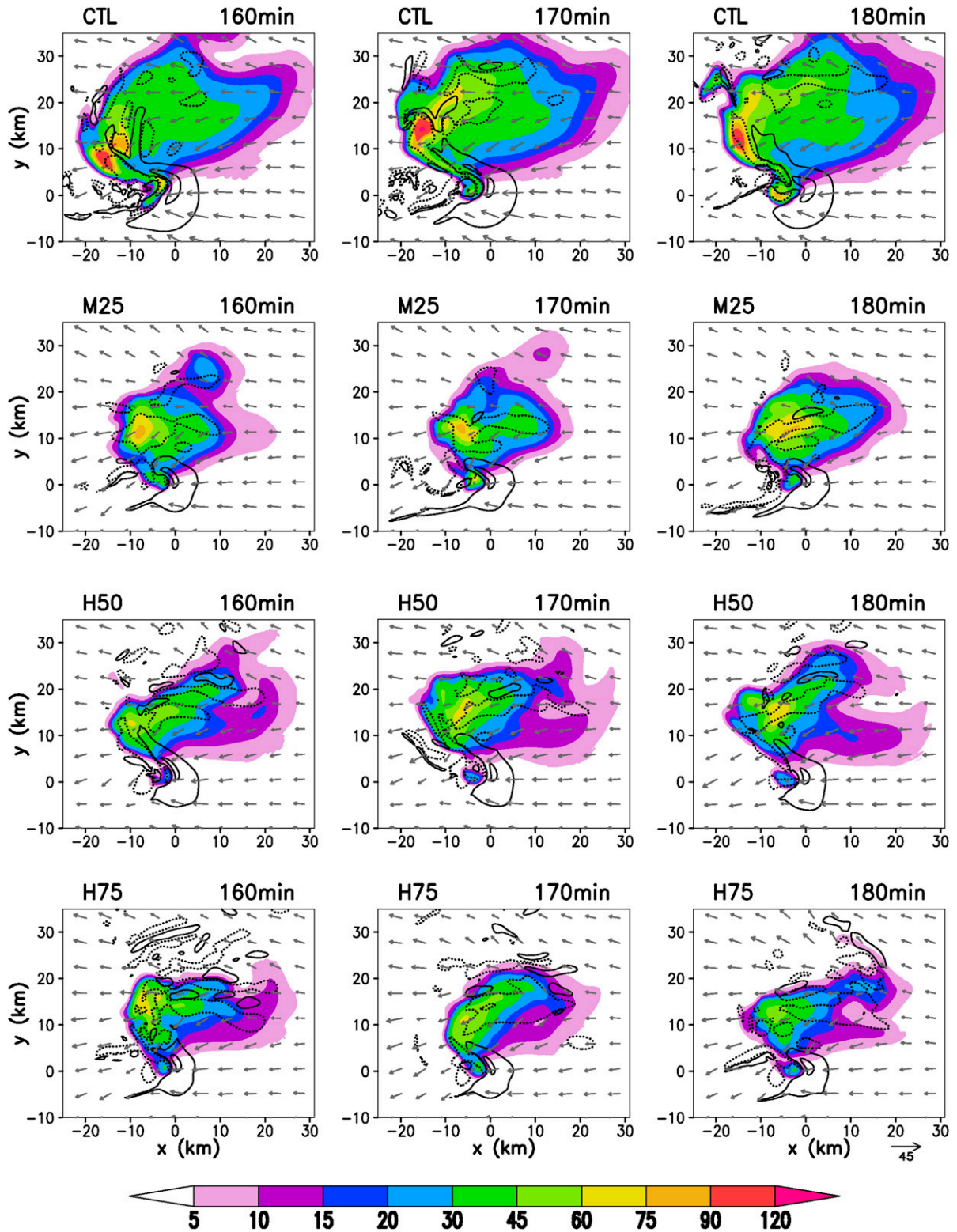


FIG. 4. Surface precipitation rate (mm h^{-1} , shaded), maximum updrafts and downdrafts within the lowest 1 km (black contours; -2 , 2 , and 10 m s^{-1} contour levels shown, negative values dashed), and storm-relative horizontal winds (m s^{-1} , gray vectors shown every eighteenth grid point; vector scale indicated in the bottom-right corner) at the lowest model level ($\sim 12 \text{ m}$ AGL) over the last 20 simulation minutes for simulations (top) CTL, (second row) M25, (third row) H50, and (bottom) H75. The horizontal axes are centered on the location of the 6-km maximum updraft at the time indicated in each panel. The figure axes are determined in this manner for the rest of the figures herein.

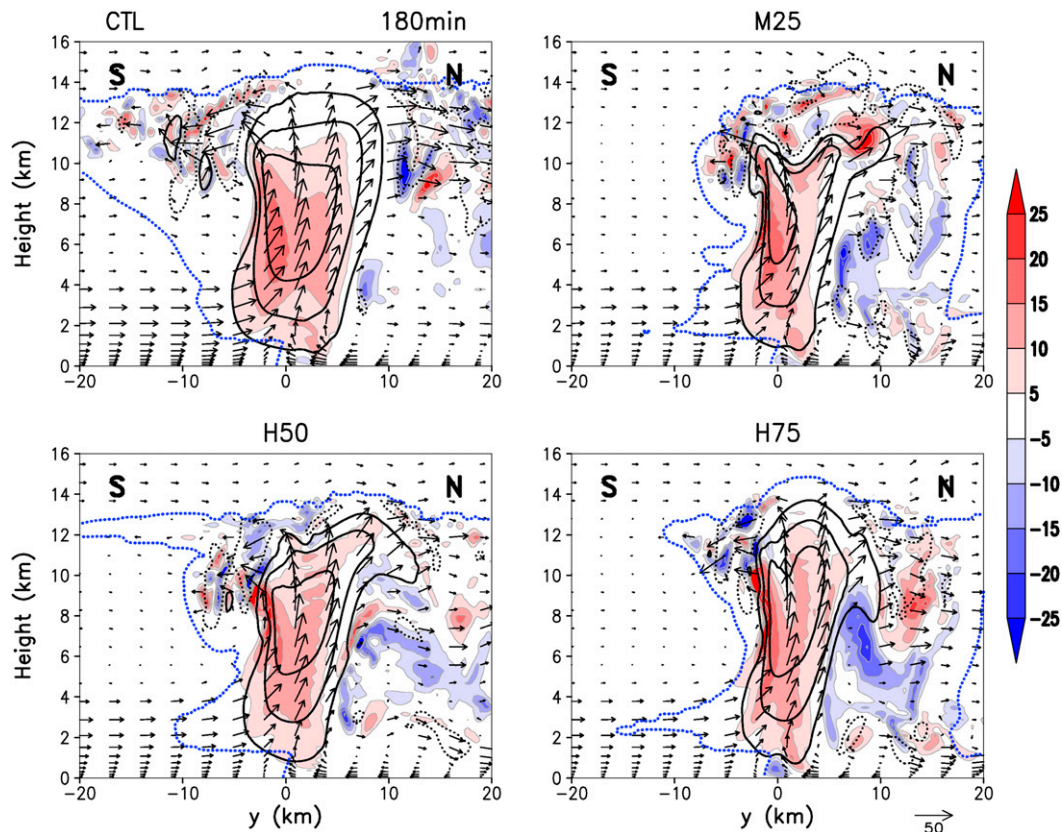


FIG. 5. South–north cross sections of vertical relative vorticity (10^{-3} s^{-1} , shaded), vertical velocity (black contours; -5 , 10 , 25 , 40 , and 55 m s^{-1} contour levels shown; negative values dashed), total condensate outline (0.01 g kg^{-1} dotted blue contour), and storm-relative v and w winds (m s^{-1} , black vectors shown every tenth grid point in the horizontal and every third grid point in the vertical; vector scale indicated in the bottom-right corner) through the 6-km maximum updraft for simulations CTL, M25, H50, and H75 at 180 min.

of point A in Fig. 6 and the positive vorticity usually to its north. The negative vorticity is the stronger and more persistent of the couplet pair. Similar midlevel vorticity couplets have been reported in previous observational (e.g., Bluestein and Gaddy 2001; Markowski 2008) and modeling (Byko et al. 2009) studies. These couplets also occur in the dry-layer supercells, although they are spatially smaller. Additionally, in the dry-layer supercells, the regions of weaker (10 – 25 m s^{-1}) updraft speeds are only contained within a narrow strip following the horseshoe shape and do not fully encompass the positive and negative vorticity couplets. These midlevel vorticity features will be discussed in relation to the microphysical processes in section 4.

Cross sections of relative humidity, total condensate mixing ratio, and storm-relative winds shown in Figs. 7 and 8 demonstrate the direct impact of the imposed dry layer on the simulated supercells. First, the dry layer impinges on the updraft between 2 and 5 km from the west (Fig. 7). The lower relative humidities in the

elevated dry layer will evaporate any existing cloud droplets on the western flank of the main updraft in the LP-like supercells, eroding the cloud edge until the flow reaches the edge of the main updraft and is diverted around it. Second, evaporation is enhanced within the forward-flank regions to the east and north of the main updrafts as precipitating hydrometeors fall through the dry layer. Consequently, precipitation rates are smaller in the FFD of the LPs (Fig. 4). Third, the dry-layer altitude sits within the deep layer southerly inflow feeding each supercell (Fig. 8). The drier air ingested into the updraft reduces the amount of vapor available for hydrometeor growth. Vapor microphysical budget terms indicate that vapor deposition is reduced in M25 and H50 relative to CTL (not shown), at times by up to about 25% at 3 and 4 km. This impacts the mass of condensate within the lower levels of the updraft.

Finally, because the updrafts are narrower in the three dry-layer supercells than in CTL, they are tilted more to the east (Fig. 7) since, at each vertical level, propagation to the right of the shear vector toward the concave side

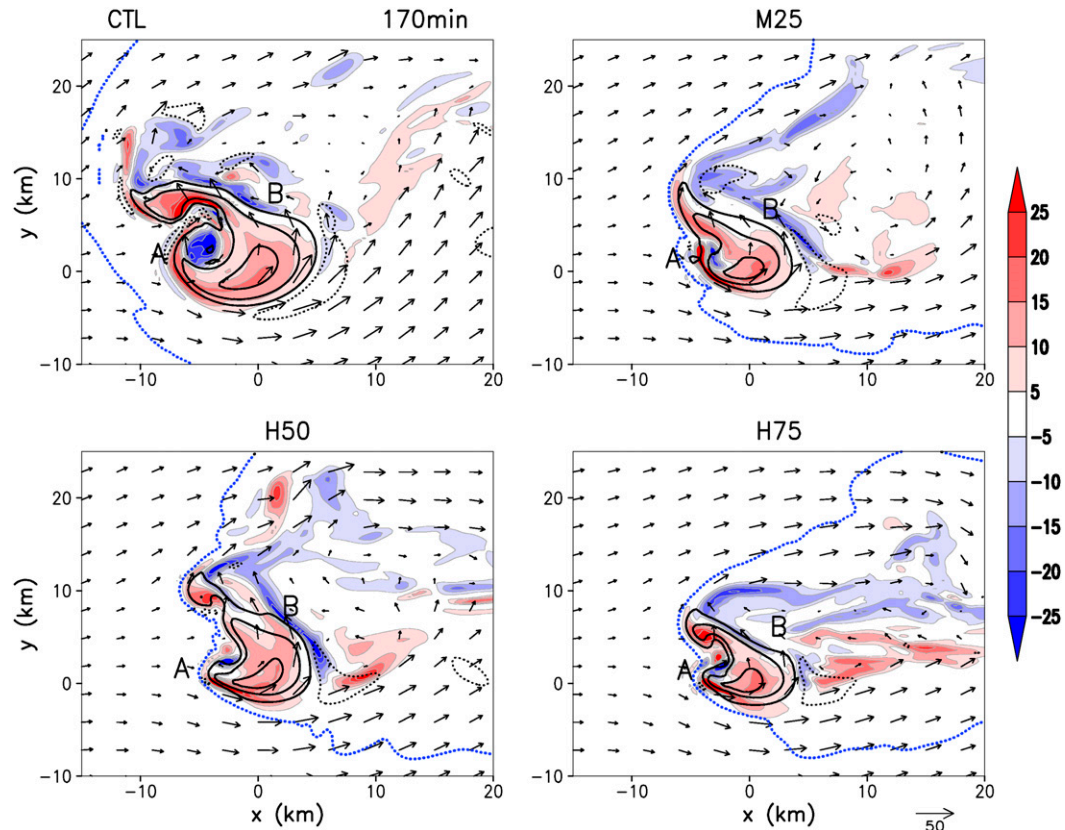


FIG. 6. Plan view at 6 km AGL, with shading, contours, and vectors as in Fig. 5, but with horizontal storm-relative wind vectors shown every tenth grid point at 170 min. Annotated points A and B are discussed in the text.

of the hodograph decreases with decreasing updraft width (Davies-Jones 2002). The tilt orientation favors hydrometeor lofting into the downshear portion of the anvil over the upshear portion. As evident in both Figs. 7 and 8, the upshear anvil is very thin or almost entirely absent in each LP supercell, and hydrometeor mixing ratios do not extend beyond the western edge of the updraft between about 4 and 10 km in M25, H50, and H75. Implications of these changes in the upshear anvil and western cloud edge for the hailstone embryo region in the classic Browning and Foote (1976) hailstone growth model, and the resulting impacts on LP supercell hail and precipitation production efficiency, are discussed in the next two sections.

c. Microphysical fields and budgets

This section discusses microphysical characteristics and budgets in the CTL, M25, and H50 simulations. The M25 and H50 LPs were chosen for the following analysis because of their similarity in total precipitation rate, updraft strength, and updraft area (Fig. 3). The magnitude of the change in PW is also most similar for these two cases. H75 is excluded because its precipitation

distribution is similar to H50 (Fig. 4). All figures within this section are presented as composites over simulation minutes 160–180 relative to the midlevel updraft center. RAMS output for these three simulations was produced every minute for this time period; thus 21 times are used for each composite. The following analysis focuses on microphysical trends within two regions of the supercell updrafts: 1) the horseshoe portion, to the west-northwest of the highest updraft speeds (simply referred to as the horseshoe from here on), and 2) the northeastern edge of the updraft. These two regions are labeled “A” and “B,” respectively, in Figs. 6 and 9–11.

The highest midlevel rain mixing ratios occur within the horseshoe (east of point A) for each of the three supercells (Figs. 9a–c). Rain mixing ratios frequently exceed 10 g kg^{-1} in the horseshoe, although the composite magnitude for CTL (Fig. 9a) is lower than this because the horseshoe of the updraft is more variable in shape for CTL than for the LPs. The largest mean rain diameters exceed 1 mm on average and are also located in the horseshoe for each supercell (Figs. 9d–f). The region of largest raindrops extends farther north of the updraft in M25 and H50 than in CTL.

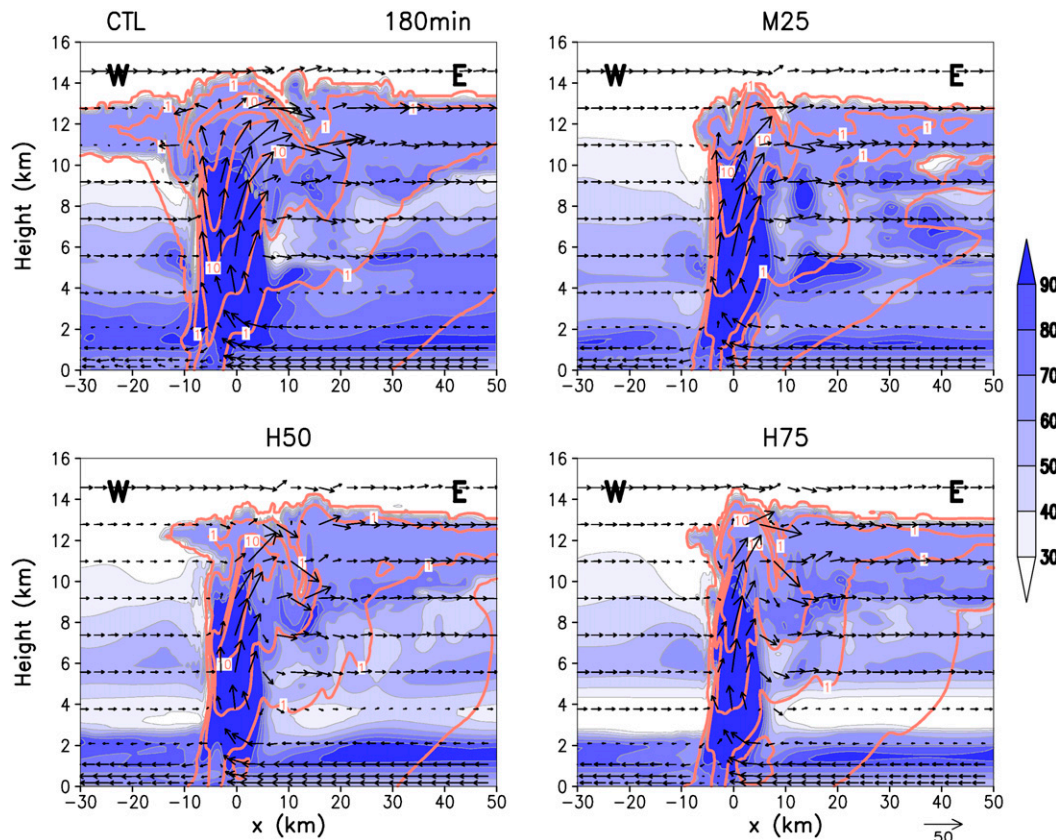


FIG. 7. West–east cross section through the location of the 6-km maximum updraft of relative humidity (% ,shaded), total condensate (orange solid contours; 5 g kg^{-1} contour interval with the 0.01 and 1 g kg^{-1} contours also shown), and storm-relative u and w winds (m s^{-1} , black vectors shown every ninth grid point in the horizontal and every sixth grid point in the vertical; vector scale indicated in the bottom-right corner) for simulations CTL, M25, H50, and H75 at 180 min.

In CTL, rain mixing ratios are negligible to the south, east, and northeast of the strongest updraft core. Conversely, the northeastern edge of the updraft near point B is characterized by a secondary strip of local maxima in rain mixing ratios and mean raindrop diameters in M25 and H50 (Figs. 9b,c,e,f). Rain mixing ratios reach 4 g kg^{-1} at times near point B for the LPs, and raindrops have diameters around $0.4\text{--}0.6 \text{ mm}$ on average. Note also that rain number concentrations are higher there than in CTL. The differences in the rain fields near point B between CTL and the LPs are persistent in time and occur through a depth of several kilometers.

Two local maxima in hail mixing ratios are present in CTL: one in the horseshoe within the $10\text{--}25 \text{ m s}^{-1}$ updraft envelope (Fig. 10a east of point A), and another to the northwest outside of the main updraft (near $x = -8$, $y = 10$). In the horseshoe, the composite hail mixing ratio exceeds 9 g kg^{-1} in CTL, but is only about 2 g kg^{-1} in H50 and is nearly negligible in M25 (Figs. 10b,c). It is not until $8\text{--}9 \text{ km}$ that hail mixing ratios within the western portion of the updraft are comparable between

CTL and the dry-layer cases (not shown). The local hail maximum that occurs to the northwest of the updraft in the CTL supercell is displaced farther east in M25 and H50. Additionally, immediately to the northeast of the updraft at point B, hail mixing ratios are up to a factor of 2 higher in the LPs compared with CTL.

Typically, the largest hail associated with CL supercells falls to the north of the updraft, whereas observations of LPs usually report hail falling from the downshear anvil—that is, northeast of the updraft (e.g., Davies-Jones et al. 1976; BP83). As noted above, the hail mixing ratio maxima outside of the updraft occurs to the northwest in the CL and to the north in the LPs. If the simulations included stronger westerly shear aloft, as is typically observed in severe weather situations, these hail locations would shift from northwest to north of the updraft in CTL and from north to northeast for the LPs, which is in agreement with observations.

In the CTL supercell, the largest mean hail diameters are collocated with the highest hail mixing ratios and large raindrops within the horseshoe (Figs. 9a, 10a,d). In

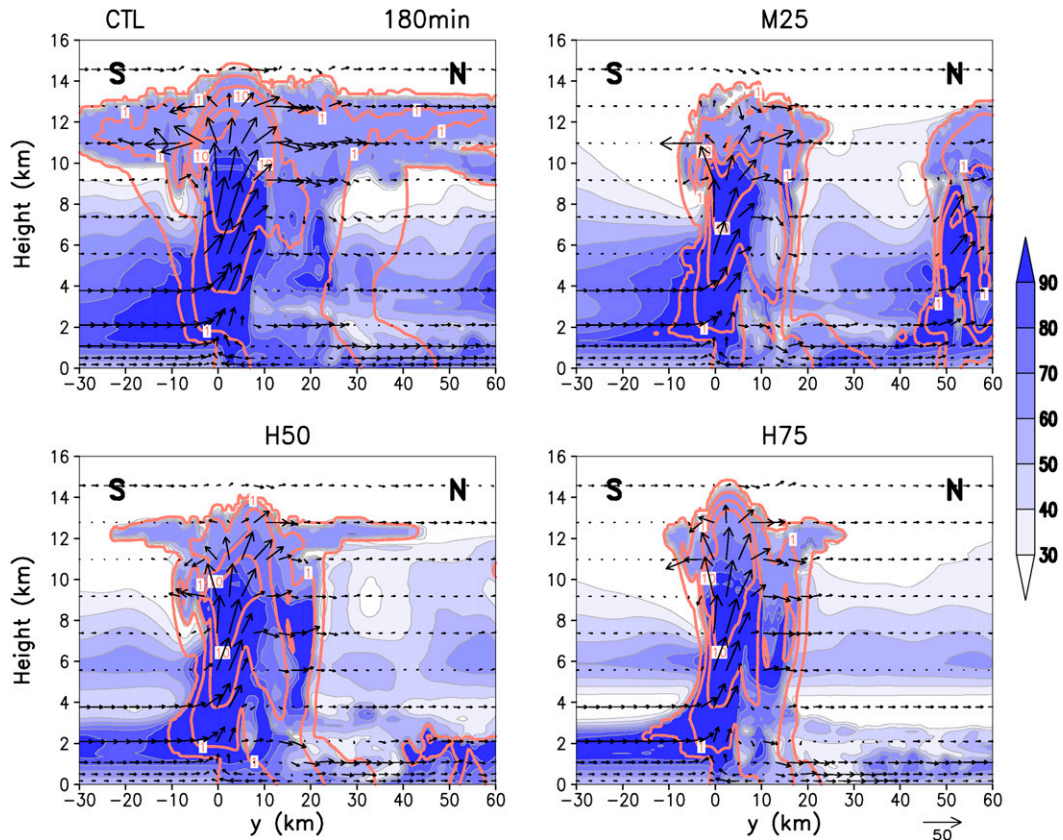


FIG. 8. As in Fig. 7, but a south–north cross section and with v and w storm-relative wind vectors.

M25 and H50, hail diameters are significantly smaller than in CTL throughout the stronger portion of the updraft. These smaller hailstones in the LPs are more easily lofted into the storm’s anvil within the strongest updraft core and are subsequently transported farther downwind of the updraft than in CTL, thereby reducing their likelihood of reaching the surface as precipitation and decreasing the precipitation efficiency of the LPs relative to CL supercells. The hail diameter differences across the updraft are also consistent with those in van den Heever and Cotton (2004), where simulations using single-moment microphysics were performed and the mean hail diameter was systematically varied. Supercell precipitation characteristics were found to move from the HP end of the spectrum toward the CL supercell structure as the mean hail diameter was decreased (their Fig. 15).

It is perhaps counterintuitive that mean hail diameters are smaller across the updraft in these simulations because observations of LPs usually report large hailstones falling from the downshear anvil. However, this may be a subjective statement in that the adjective “large” is relative to the typically reported lack of rain occurring with these storms, as pointed out in Beatty et al. (2008). Additionally,

observations of mean hail diameters within an LP supercell and a CL supercell occurring in a similar environment do not exist to the authors’ knowledge, and a climatology of typical hail sizes associated with LPs and CLs is not available owing to the relative scarcity of LP observations.

Differences in hail number concentrations arise between the CTL and dry-layer supercells near both points A and B (Fig. 10g–i). In CTL, a region of small hailstones with number concentrations between 500 and 1000 kg^{-1} occurs just east of point A outside the 10 m s^{-1} updraft contour for all the individual times within this analysis period, although it only faintly appears in the composite because the CTL horseshoe shape changes in time, as previously mentioned. The corresponding hail mixing ratios are 2–3 g kg^{-1} there. The location of this region corresponds to the location of the embryo curtain in the Browning and Foote (1976) model for hailstone growth—a source region for hailstone embryos on a supercell’s right flank—and is absent in M25 and H50 at this altitude (see also Figs. 7–8). There are also differences in hail number concentrations near point B; hail concentrations are enhanced in the dry-layer supercells immediately outside of the updraft to the east-northeast.

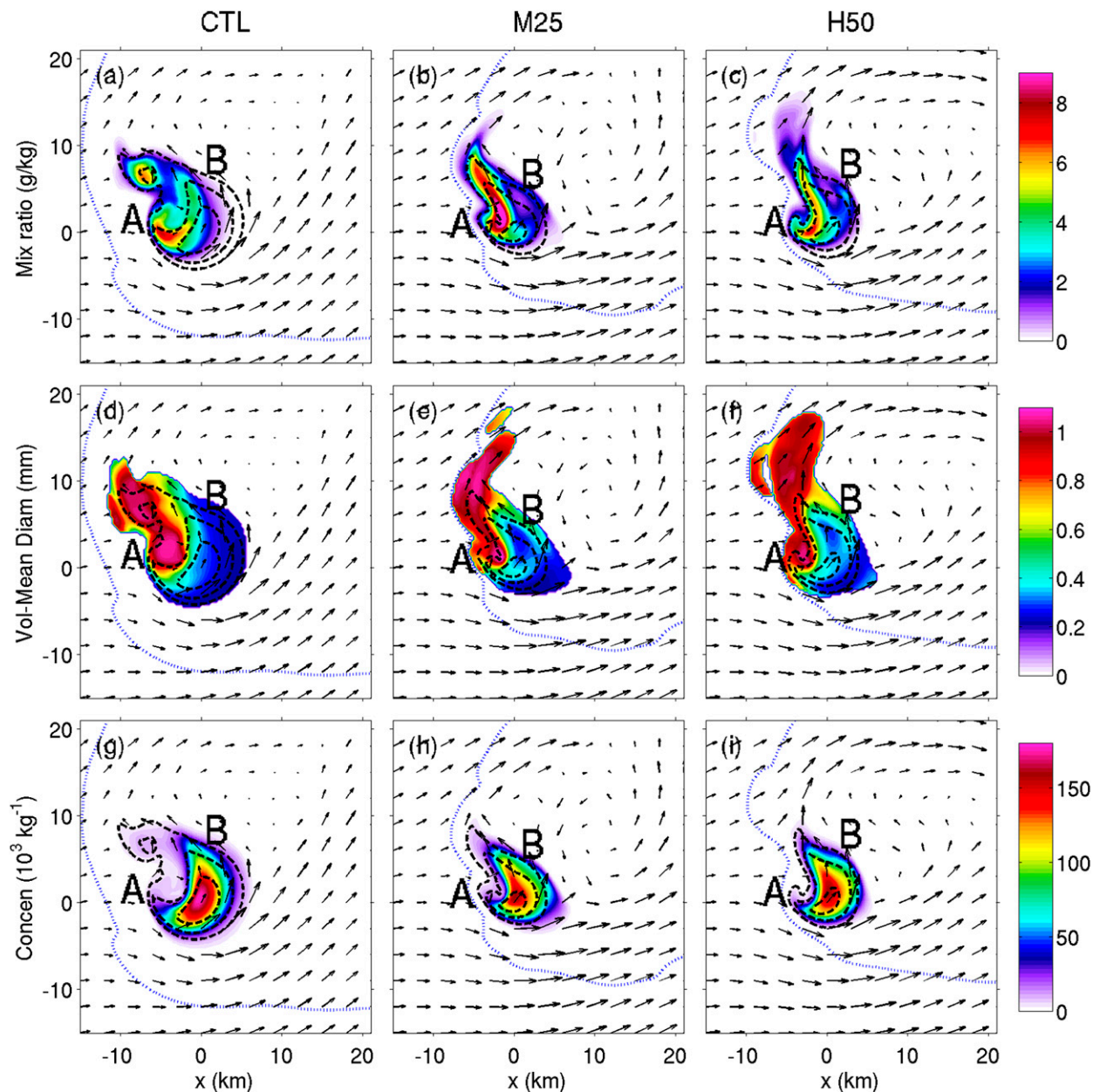


FIG. 9. Composite plan view at 6 km AGL of (a)–(c) rain mixing ratio (g kg^{-1}), (d)–(f) volume-mean rain diameter (mm, only where mixing ratio exceeds 0.05 g kg^{-1}), and (g)–(i) rain number concentration (10^3 kg^{-3}). All panels also show vertical velocity (10, 25, and 40 m s^{-1} , black dashed contours), total condensate outline (0.01 g kg^{-1} , blue dotted contour), and storm-relative horizontal winds (m s^{-1} , black vectors shown every tenth grid point) for simulations (left) CTL, (center) M25, and (right) H50. All fields shown in Figs. 9–12 are composites taken from 160–180 min (21 times) relative to the intensity-weighted updraft center at 6 km AGL; axis numberings are distances (km) from the updraft center. Annotated points A and B are discussed in the text.

Microphysical process budgets afford a closer look at the differences between the rain and hail fields in CTL, M25, and H50. Within the horseshoe, to the east of point A, riming rates are substantially larger in CTL than in the dry-layer supercells, especially at 6 km (Figs. 11a–f). Moreover, the riming rates with the horseshoe for CTL are larger in magnitude by several grams per kilogram

per minute at individual times than is indicated in the composite. In the dry-layer supercells, riming rates are enhanced at point B along the northeastern side of the updraft relative to CTL, especially at 7 km (Figs. 11a–f). Collision and coalescence processes are also more efficient there (Figs. 11h,i), whereas cloud-to-rain conversion rates are negligible along the entire southern, eastern, and

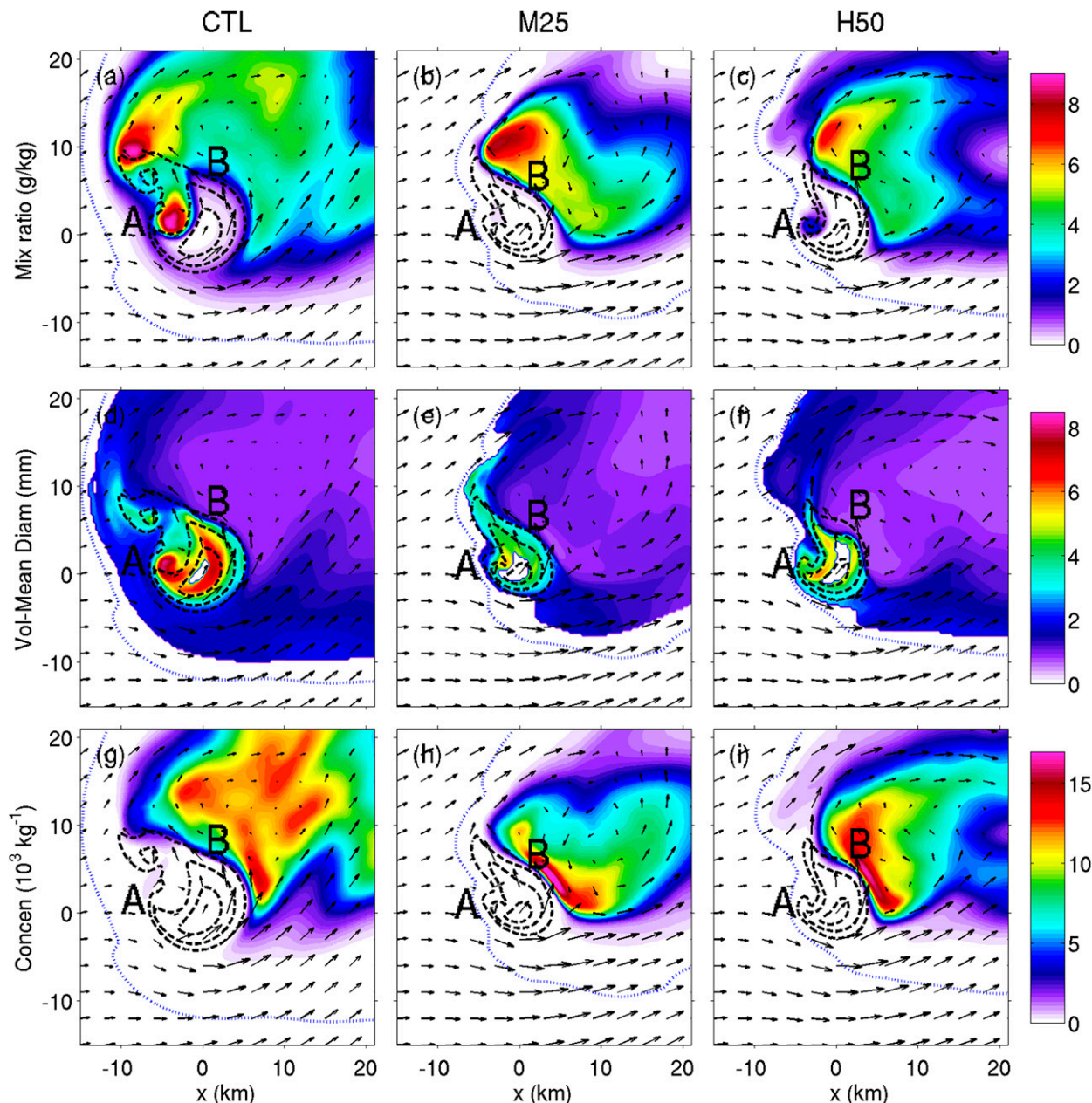


FIG. 10. As in Fig. 9, but for (a)–(c) hail mixing ratio (g kg^{-1}), (d)–(f) volume-mean hail diameter (mm), and (g)–(i) hail number concentration (10^3 kg^{-1}).

northeastern edges of the CTL supercell updraft (Fig. 11g). The more efficient rain production south of point B in M25 and H50 is collocated with the locally higher rain mixing ratios and larger raindrops. The implications of these different process rates for hail growth are discussed next.

4. Hail growth mechanisms

In this section, hailstone growth processes are discussed in relation to the aforementioned differences in the

microphysical fields and budgets, first in the context of the Browning and Foote (1976) hailstone growth model. In this model, small frozen hydrometeors, or hailstone embryos, fall from the back-sheared anvil (referred to as the embryo curtain) and become reingested in the updraft, where they accrete liquid water during their final ascent through the updraft. The largest hailstones grow in a favored region of moderate updraft strength, where the hailstone fall velocity approximately balances the updraft speed.

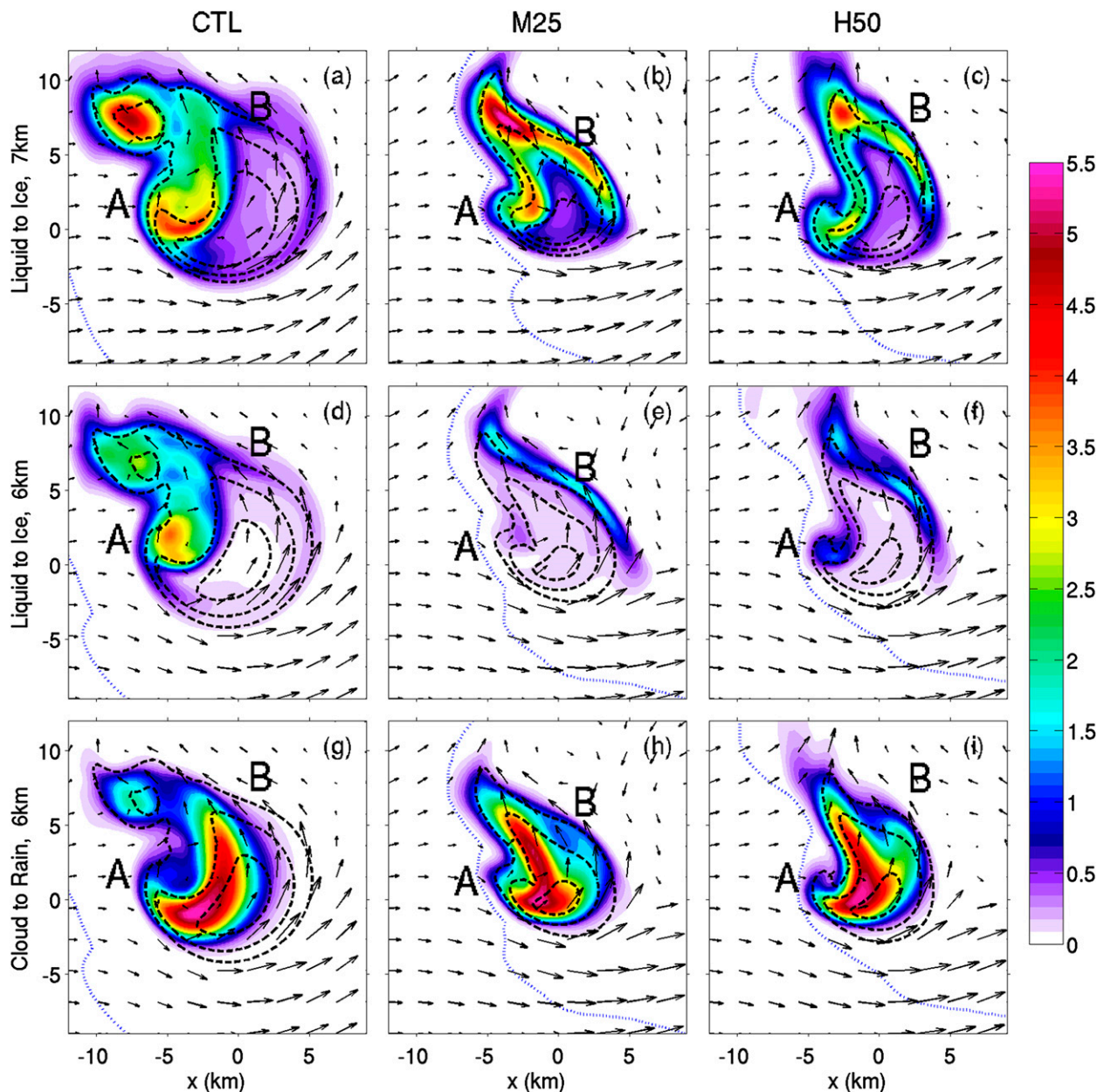


FIG. 11. Composite plan views of microphysical budget process rates ($\text{g kg}^{-1} \text{min}^{-1}$, shaded) for cloud and rainwater collected by all ice species at (a)–(c) 7 and (d)–(f) 6 km AGL, and (g)–(i) conversion of cloud to rainwater by collection at 6 km AGL. Also shown are updraft speeds (10, 25, and 40 m s^{-1} , dashed black contours) and the total condensate outline (0.01 g kg^{-1} , blue dotted contour) for simulations (left) CTL, (center) M25, and (right) H50. Composite fields are calculated as in Fig. 9. Annotated points A and B are discussed in the text.

In the CTL classic-type supercell, high riming rates, high rain and hail mixing ratios, and large rain and hail diameters are all collocated within the horseshoe where updraft speeds are moderate ($\sim 10\text{--}25 \text{ m s}^{-1}$). Hailstone fall speeds in RAMS are given by the power law formula $v_t = 152.1D^{0.497}$, where v_t is the terminal velocity (m s^{-1}) and D is the mean hail diameter (m), following Mitchell (1996). The highest mean hail diameters contributing to the composite in Fig. 10 frequently exceed 9 mm, for

which the corresponding hailstone fall speed is approximately 15 m s^{-1} . These fall speeds are relatively well balanced by the updraft, permitting longer hailstone residence times. Furthermore, these signals are collocated with the anticyclonic and cyclonic vorticity couplet (Fig. 6). Storm-relative wind speeds are weak, and the flow orientation associated with the vorticity couplet prevents growing hailstones from advecting horizontally around the mesocyclone, further extending hailstone

residence times in this region. The superposition of high hydrometeor mixing ratios and the vorticity couplets resembles the mechanism for type I descending reflectivity core (DRC) formation within a “stagnation zone” (Rasmussen et al. 2006; Byko et al. 2009). All of these signals together indicate that in the CTL supercell, efficient large hailstone growth mechanisms are at work within the horseshoe. Hailstone embryos originate within the embryo curtain resulting from the backsheared anvil, as suggested in the Browning and Foote (1976) model. Hail that grows large enough in the horseshoe may begin falling relative to the updraft, advecting either cyclonically around the southwestern side of the updraft and contributing to the RFD precipitation (e.g., Knight and Knupp 1986) or anticyclonically to the northern side of the updraft, contributing to the precipitation within the main hailstone fallout region in the CL supercell structure (Browning 1964; Lemon and Doswell 1979; Browning and Foote 1976).

Although the vorticity couplets and local rain mixing ratio maxima are also present in the horseshoe for M25 and H50, the relative lack of high hail mixing ratios and large hail diameters combined with the small backsheared anvil, absence of the right-flank hailstone embryo region, and reduced area of moderate updraft speeds near the horseshoe indicate that the classic Browning and Foote (1976) hailstone growth model is much less efficient in LP supercells. As described in the previous section, the northeastern side of the updraft in M25 and H50 contains higher rain and hail mixing ratios, larger raindrops, and enhanced riming relative to CTL. Interestingly, the enhanced riming in the LPs is collocated with a strip of negative relative vorticity (Fig. 6, point B). Storm-relative flow associated with this vorticity keeps hydrometeors, whether raindrops or hailstones, along the edge of the updraft as they are advected cyclonically around the eastern side of the mesocyclone. Therefore, it appears that another hail growth pathway exists along the northeastern edge of the updraft that is more efficient in LP supercells. This mechanism is hypothesized to work in the following way.¹

¹ Hailstone trajectories cannot be computed quantitatively because of the uncertainties associated with accurately representing such trajectories within cloud-resolving models that utilize bulk microphysical schemes. Such uncertainties are further enhanced when using the RAMS bin-emulating bulk scheme because it (i) represents the hydrometeor size distributions with a continuous function rather than discrete bins, (ii) allows the mass and number distributions to fall with different fall speeds within a time step, and (iii) utilizes bin-emulating sedimentation procedures through the use of lookup tables. Therefore, composite microphysical fields and process rates are used to demonstrate the CL and LP hail growth mechanisms instead.

More and larger raindrops are available along the northeastern side of the updraft in the LP supercells (Figs. 9b,c,e,f), owing in part to (i) advection cyclonically around the mesocyclone from the horseshoe, given the lack of hail to collect rain by riming in this region (Fig. 10), and (ii) enhanced collision and coalescence processes (Figs. 11h,i) due to the larger raindrops present and thus higher collection efficiencies. Greater hail mixing ratios and higher number concentrations of smaller hailstones are also located just outside of the northeastern updraft edge (Fig. 10) due to the weaker storm-relative winds to the north and east of the main updraft at middle and upper levels (e.g., Figs. 7 and 8). Hail embryos that are not transported within the strongest core of the updraft and out into the anvil region downwind, but instead fall out on the northern and eastern peripheries of the updraft at upper levels, will fall closer to the midlevel updraft where they may be recirculated into the updraft edge by the storm-relative flow. Note that the composite storm-relative wind vectors around point B, outside of the main updraft, have a northerly or easterly component in M25 and H50, whereas they do not in CTL (Figs. 9–11). The subsequent combination of larger raindrops and more numerous small hailstones enhances the riming process, thereby producing more efficient hailstone growth along the northeastern updraft edge in the LPs before the hailstones fall out in the FFD region.

Previous studies of hail growth processes support the mechanisms in this proposed LP supercell hailstone growth model. Nelson (1983) indicates that hailstones can grow to sufficient size in a single traverse through the updraft and that hail growth tends to occur at a nearly constant altitude. Temperatures within the updraft near 6 and 7 km in M25 and H50, where the strongest riming signature is seen along the northeastern updraft edge, fall within the -10° to -25°C zone that is efficient for hailstone growth (Foote 1984) (Fig. 12). Last, Rasmussen and Heymsfield (1987) describe a supercell case in which hailstone growth likely occurred across the updraft core or along the updraft edges; hailstone embryos were thought to originate from the updraft fringes.

In summary, because of the differences in the updraft tilt and shape and the dry-layer impacts on the cloud edge, a spatial reorientation of the hydrometeors (Fig. 12) favors a different dominant midlevel hail growth mechanism in LPs compared with CL supercells. As evidenced in both the plan view and the cross section in Fig. 12, the most significant overlap regions between the hail and rain mixing ratios within the prime temperature growth zone shift from the western and southwestern sides of the updraft in the CL supercell to the northeastern side in the LP supercells. Therefore, as described

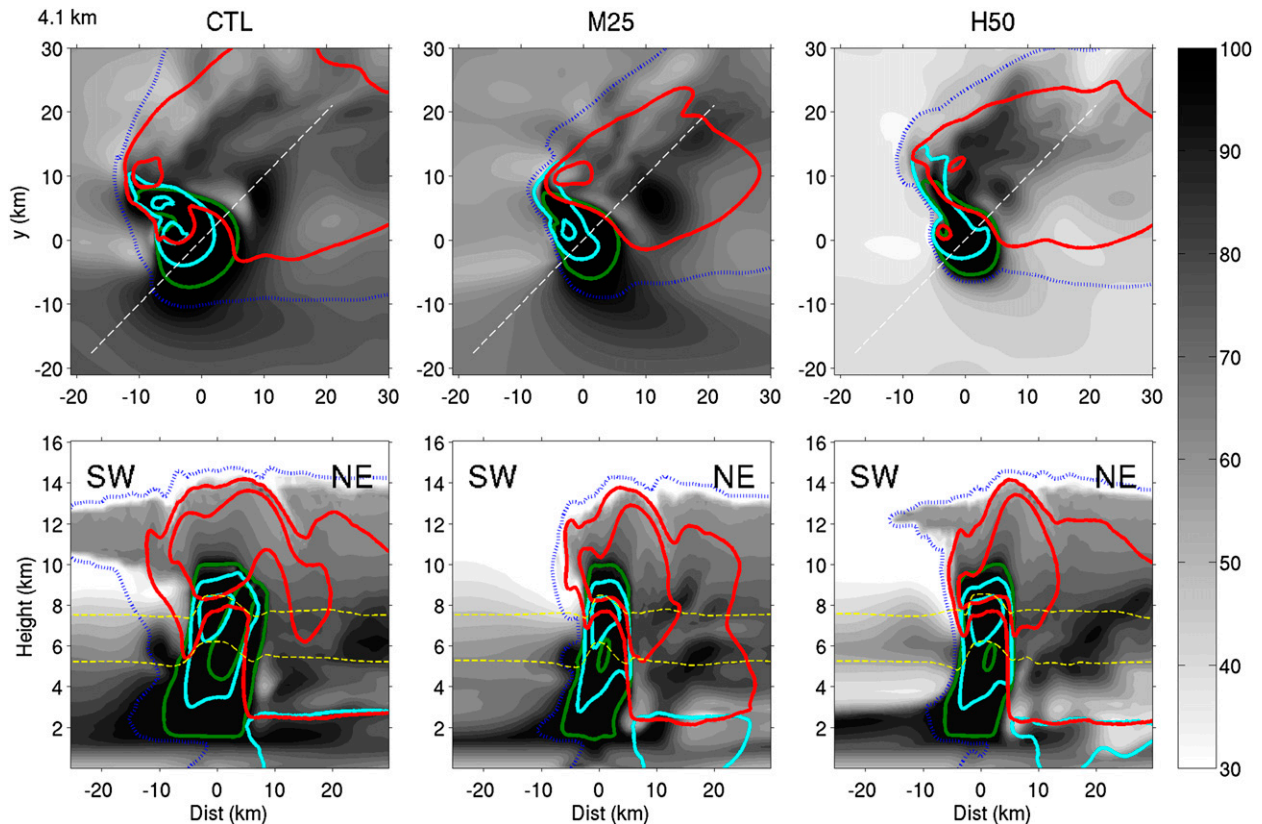


FIG. 12. (top) Composite plan view at 4.1 km AGL and (bottom) southwest–northeast cross sections of relative humidity (shaded), cloud mixing ratio (cyan solid contours), drizzle plus rain mixing ratio (green solid contours), hail mixing ratio (red solid contours), temperature (-10° and -25°C , yellow dashed contours), and total condensate outline (0.01 g kg^{-1} , blue dotted contour) for simulations (left) CTL, (center) M25, and (right) H50. The 0.5 and 5 g kg^{-1} mixing ratio contours are shown. Composite fields are calculated as in Fig. 9. White dashed lines in the plan views indicate the location of the cross sections.

above, hailstone growth is favored along the eastern and northeastern edges of the mesocyclone in the LPs. The heaviest precipitation is also favored to the north and east of the updraft within the FFD region, while the RFD precipitation rates are much lighter. The shift in hydrometeor mixing ratio distributions and relative importance of the different hailstone growth mechanisms within CL and LP supercells can therefore explain their variations in precipitation distributions (Fig. 4). The two hail growth mechanisms and their associated hailstone embryo source regions, areas of highest riming rates, and resulting surface precipitation distributions are summarized in the schematic presented in Fig. 13.

5. Discussion

The simulations described above demonstrate that two hail growth mechanisms are evident in each supercell, although their relative importance varies substantially between storm types. While the classic Browning and Foote (1976) model is clearly evident in the CL supercell,

a weak riming signal within the horseshoe is also present in the dry-layer supercells at 6 km (Fig. 11). A hail overhang region also appears on the southwestern side of the updraft in M25 and H50 within the prime temperature zone for hail growth, where it overlaps slightly with cloud and rainwater (Fig. 12). However, the magnitude and vertical extent of this hail overhang is greatly reduced compared to CTL. Additionally, the riming signal on the northeastern updraft edge is present in the CTL supercell, but it is much weaker than in M25 and H50. Therefore, although substantial differences in their microphysical structures are evident, it does not appear that LP and CL supercells are distinct storm types from this point of view, especially given the similarities in their updraft and vorticity structures. In other words, supercell morphology is characterized by a continuous spectrum rather than discrete types (e.g., Doswell et al. 1990; RS98).

Some of the previously hypothesized storm morphology discrimination mechanisms can be addressed with the results from these simulations. Several hypotheses,

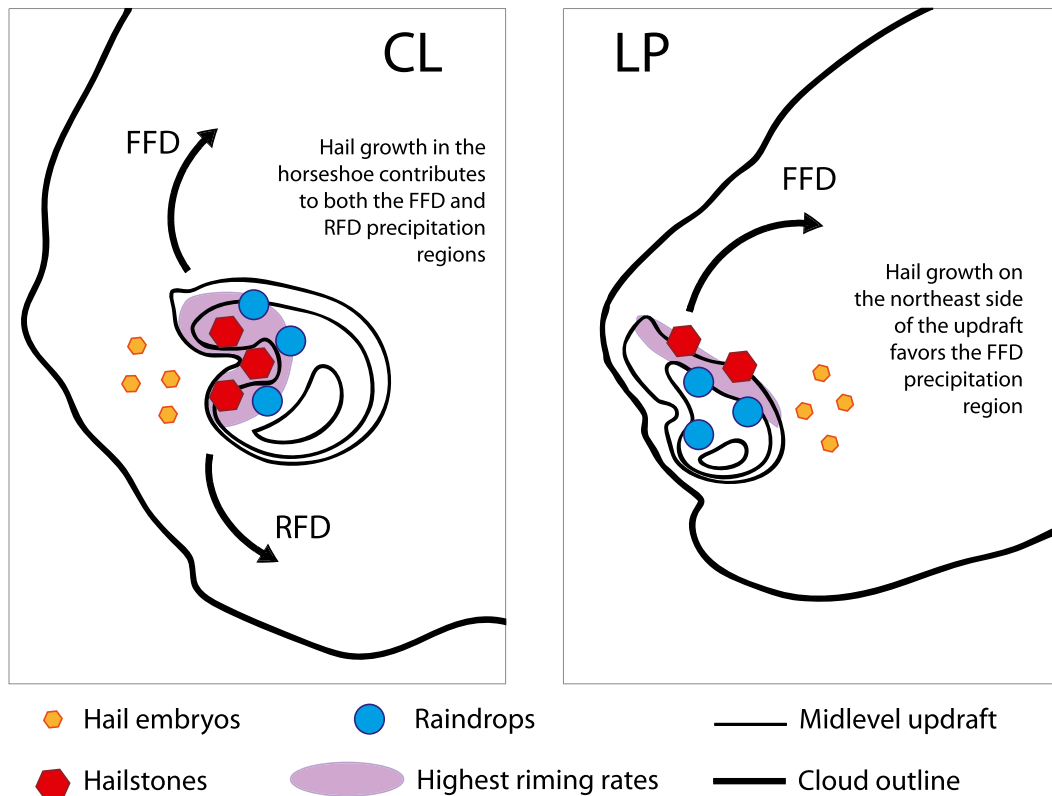


FIG. 13. Schematic diagram of the primary midlevel hail growth mechanisms in (left) classic and (right) low-precipitation supercells. The cloud outline (0.01 g kg^{-1} total condensate) and midlevel updraft speeds ($10, 25, \text{ and } 45 \text{ m s}^{-1}$) are taken from composite fields at 7 km for CTL and M25.

including those of Brooks et al. (1994) and RS98, suggest that storm morphology depends on the environmental wind shear profile and resulting differences in storm-relative winds. It was shown that differences in storm-relative winds are in fact central to the differences in hydrometeor distributions and hail growth mechanisms for CL and LP supercells. However, the changes in the storm-relative winds are not due to differences in the environmental wind profile, as this was kept identical in each simulation. Rather, the storm-relative wind differences are due purely to each storm’s own motion and the storm-scale-generated flow field. RS98 also speculated that supercell archetype may in fact depend on the storm motion itself.

BP83 hypothesized that storm morphology may depend on the initial bubble size owing to differences in low-level moisture structure near the dryline. The results presented in this study suggest that the moisture content above the well-mixed boundary layer is more important for strong LP supercell formation than low-level moisture content and hence do not support this hypothesis, since neither the initial bubble size nor the vapor mixing ratio within the well-mixed layer were varied.

In these simulations, supercell updrafts were weaker and more unsteady when the dry layer depleted moisture from the well-mixed boundary layer (M and L simulations), consistent with the findings in BP83 and McCaul and Cohen (2002). However, it is not known how the results in this study translate to different CAPE and shear combinations. For instance, McCaul and Cohen (2002) demonstrated that when the lifting condensation level increased, simulated storms were stronger but tended more toward outflow dominance, depending on the CAPE. They also used a curved hodograph in their simulations, but the magnitude of the shear was weaker than used in this study. Gilmore and Wicker (1998) found that simulated supercells were more susceptible to outflow dominance when midlevel dryness was increased, when dry layers were lower in altitude, and when the vertical shear was weaker. Their study utilized larger CAPE and a straight hodograph. Future research should therefore test the robustness of simulated supercell morphology sensitivity to the presence of dry layers under a suite of different CAPE and shear profiles. Moreover, James and Markowski (2010) showed that the impact of midlevel dryness on deep convection is sensitive to the microphysical scheme utilized. It would

therefore also be interesting to investigate LP and CL supercell dynamical and microphysical structure using a triple-moment hail scheme, which would allow the hail size distribution width to vary in addition to mass and number concentration (Loftus 2012).

LP supercells are known for their difficulty to detect with radar (BD79). Given the differences in the hail mixing ratio distribution in the plan views of Fig. 12, it is clear that the classic hook-echo shape often used to identify supercells would be much less distinct for LPs, especially if the storm is far enough away from the radar that the lowest elevation scan is sampling the midlevels of the storm, since most of the precipitation falls out ahead of the updraft. The slower and weaker motion off the right of the hodograph in these simulated LPs, which has also been noted in observations (BD79; BP83), may be a useful tool for forecasters to identify LP supercells that have ambiguous radar signals, particularly if model forecast soundings contain elevated dry layers. It is noteworthy that the differences in storm motion are supported by the theory presented in Davies-Jones (2002). For curved hodographs, propagation off the hodograph decreases with decreasing updraft width by virtue of changes to the spatial distribution of the non-hydrostatic vertical pressure gradient force, or upward forcing, induced by linear interactions between the updraft and the environmental shear. Since LPs have narrower updrafts, it may be expected that their deviant rightward storm motions are smaller. More observations are necessary, perhaps even stratified by hodograph curvature, to ascertain whether the trend in storm motion is robust.

The relative changes in PW in relation to storm morphology may also be of interest to forecasters (Table 3). In this study, environments in which PW was decreased by 19% or greater from CTL were not supportive of strong supercells (M50, M75, L50). The H25 RM supercell characteristics were between those of a CL and an LP; the decrease in PW was only about 6% for this case. The strong LPs formed when PW was reduced by 10%–20% (M25, H50, and H75), although only if the dry layer was sufficiently elevated. BP83 and RS98 also found differences in PW for different supercell types. However, it should be emphasized that absolute PW magnitude should not be used to rank storm type because 1) as demonstrated here, supercell morphology is more sensitive to the vertical distribution of moisture, and 2) PW is sensitive to the low-level moisture content, which was not varied in this study. Last, some observations have reported supercell morphology transition within the supercell life cycle (Bluestein and Woodall 1990). According to the findings presented here, supercells may evolve away from the LP end of the spectrum if they form along

the dryline or high plains and propagate into environments with higher PW due to deeper mixed layers or higher midlevel moisture content. This may occur in the far-dryline environment as surface elevation decreases and the influence of the elevated mixed layer diminishes.

6. Summary

The goal of this study has been to investigate the sensitivity of simulated supercell morphology to the vertical distribution of moisture. A suite of simulations was performed in which dry layers of varying magnitudes and altitudes were added to an environment characterized by deep moisture content. The moist profile produced a CL supercell. Though some of the dry-layer scenarios were not supportive of sustained convection, strong and steady LP supercells formed when the imposed dry layer was elevated or weak (simulations H25–75 and M25).

The dry layers erode the cloud edge west of the updraft in the simulated LP supercells, which have narrower updrafts that are tilted more toward the east compared to the CL supercell. This combination favors a downshear distribution of hydrometeors and severely limits the upshear anvil extent and hail overhang in the LP storm types. Hail diameters are smaller throughout the updraft in the LPs, allowing them to be lofted more easily into the anvil. Additionally, the dry layers enhance evaporation of precipitation. As a result of these differences, lighter precipitation is found throughout most of the FFD region in the LPs. LP supercells therefore represent the lowest-precipitation-efficiency storm type within the supercell spectrum, as first suggested by BP83. Despite the large changes to the microphysical structure, the main dynamical features, including the strength and structure of the updraft and the vorticity, are similar between the LP and CL supercells.

It was demonstrated through the use of microphysical fields and process budgets that different hail growth mechanisms are important in LPs relative to CL supercells, as summarized in Fig. 13. At midlevels, the primary hail growth region is located along the northeastern edge of the updraft in LPs, whereas in CL supercells, efficient hail growth is preferred within the horseshoe of the updraft. The LP hail growth mechanism favors the FFD precipitation region and assists in explaining the resulting differences in the surface precipitation distribution between CLs and LPs.

The sensitivity of supercell morphology to the presence of elevated dry layers makes sense considering the environment in which LP supercells typically form—namely along the dryline and the high plains—and the

fact that LP supercells are usually isolated or the farthest upwind in a line of storms. Supercells that form in these environments are more likely to draw in unmodified, drier low- to midlevel air that has not been preconditioned by previous convection. Additionally, although not investigated in this study, LPs may also be the most upwind supercells owing to possible “seeding” of downwind storms by anvil precipitation (RS98) into the right-flank embryo curtain.

High-resolution simulations of LPs and CLs occurring under similar environments with similar updraft strengths and using a sophisticated microphysical scheme have not been previously performed to the authors’ knowledge. While new observations of LPs—such as those that can be obtained through the use of polarimetric radar—are needed to validate the findings here, the results of this study provide unique new insights into the dynamical and microphysical structure of LP supercells, which has not been possible with the limited observational data available to date.

Acknowledgments. The authors gratefully acknowledge the Cooperative Institute for Research in the Atmosphere (CIRA) for the Graduate Student Fellowship that supported this research. The insightful comments from two anonymous reviewers, which resulted in an improved manuscript, are greatly appreciated. The authors also thank Dr. Robert B. Seigel (University of Miami) for his work on the distributed memory parallelization code within RAMS, which made possible running the simulations on Yellowstone. High-performance computing support from Yellowstone (ark:/85065/d7wd3xhc) was provided by NCAR’s Computational and Information Systems Laboratory, sponsored by the National Science Foundation.

REFERENCES

- Beatty, K., E. N. Rasmussen, and J. M. Straka, 2008: The supercell spectrum. Part I: A review of research related to supercell precipitation morphology. *Electron. J. Severe Storms Meteor.*, **3** (4), 1–21. [Available online at <http://www.ejssm.org/ojs/index.php/ejssm/article/viewarticle/44/45>.]
- Bluestein, H. B., 1984: Further examples of low-precipitation severe thunderstorms. *Mon. Wea. Rev.*, **112**, 1885–1888, doi:10.1175/1520-0493(1984)112<1885:FEOLPS>2.0.CO;2.
- , and C. R. Parks, 1983: A synoptic and photographic climatology of low-precipitation severe thunderstorms in the Southern Plains. *Mon. Wea. Rev.*, **111**, 2034–2046, doi:10.1175/1520-0493(1983)111<2034:ASAPCO>2.0.CO;2.
- , and G. R. Woodall, 1990: Doppler-radar analysis of a low-precipitation severe storm. *Mon. Wea. Rev.*, **118**, 1640–1665, doi:10.1175/1520-0493(1990)118<1640:DRAOAL>2.0.CO;2.
- , and S. G. Gaddy, 2001: Airborne pseudo-dual-Doppler analysis of a rear-inflow jet and deep convergence zone within a supercell. *Mon. Wea. Rev.*, **129**, 2270–2289, doi:10.1175/1520-0493(2001)129<2270:APDDAO>2.0.CO;2.
- Brooks, H. E., and R. B. Wilhelmson, 1992: Numerical simulation of a low-precipitation supercell thunderstorm. *Meteor. Atmos. Phys.*, **49**, 3–17, doi:10.1007/BF01025398.
- , C. A. Doswell, and R. B. Wilhelmson, 1994: The role of midtropospheric winds in the evolution and maintenance of low-level mesocyclones. *Mon. Wea. Rev.*, **122**, 126–136, doi:10.1175/1520-0493(1994)122<0126:TROMWI>2.0.CO;2.
- Browning, K. A., 1964: Airflow and precipitation trajectories within severe local storms which travel to the right of the winds. *J. Atmos. Sci.*, **21**, 634–639, doi:10.1175/1520-0469(1964)021<0634:AAPTWS>2.0.CO;2.
- , 1977: The structure and mechanism of hailstorms. *Hail: A Review of Hail Science and Hail Suppression*, Meteor. Monogr., No. 38, Amer. Meteor. Soc., 1–43.
- , and G. B. Foote, 1976: Airflow and hail growth in supercell storms and some implications for hail suppression. *Quart. J. Roy. Meteor. Soc.*, **102**, 499–533, doi:10.1002/qj.49710243303.
- Burgess, D. W., and R. P. Davies-Jones, 1979: Unusual tornadic storms in eastern Oklahoma on 5 December 1975. *Mon. Wea. Rev.*, **107**, 451–457, doi:10.1175/1520-0493(1979)107<0451:UTSIEO>2.0.CO;2.
- Byko, Z., P. Markowski, Y. Richardson, J. Wurman, and E. Adelman, 2009: Descending reflectivity cores in supercell thunderstorms observed by mobile radars and in a high-resolution numerical simulation. *Wea. Forecasting*, **24**, 155–186, doi:10.1175/2008WAF2222116.1.
- Cai, H., W.-C. Lee, T. M. Weckwerth, C. Flamant, and H. V. Murphey, 2006: Observations of the 11 June dryline during IHOP_2002—A null case for convection initiation. *Mon. Wea. Rev.*, **134**, 336–354, doi:10.1175/MWR2998.1.
- Cotton, W. R., and Coauthors, 2003: RAMS 2001: Current status and future directions. *Meteor. Atmos. Phys.*, **82**, 5–29, doi:10.1007/s00703-001-0584-9.
- Davies-Jones, R., 2002: Linear and nonlinear propagation of supercell storms. *J. Atmos. Sci.*, **59**, 3178–3205, doi:10.1175/1520-0469(2003)059<3178:LANPOS>2.0.CO;2.
- , D. W. Burgess, and L. R. Lemon, 1976: An atypical tornado-producing cumulonimbus. *Weather*, **31**, 337–347, doi:10.1002/j.1477-8696.1976.tb07449.x.
- DeMott, P. J., and Coauthors, 2010: Predicting global atmospheric ice nuclei distributions and their impacts on climate. *Proc. Natl. Acad. Sci. USA*, **107**, 11 217–11 222, doi:10.1073/pnas.0910818107.
- Doswell, C. A., and D. W. Burgess, 1993: Tornadoes and tornadic storms: A review of conceptual models. *The Tornado: Its Structure, Dynamics, Prediction, and Hazards*, Geophys. Monogr., Vol. 79, Amer. Geophys. Union, 161–172.
- , A. R. Moller, and R. Przybylinski, 1990: A unified set of conceptual models for variations on the supercell theme. Preprints, *16th Conf. Severe Local Storms*, Kananaskis Park, AB, Canada, Amer. Meteor. Soc., 40–45.
- Droegemeier, K. K., S. M. Lazarus, and R. Davies-Jones, 1993: The influence of helicity on numerically simulated convective storms. *Mon. Wea. Rev.*, **121**, 2005–2029, doi:10.1175/1520-0493(1993)121<2005:TIOHON>2.0.CO;2.
- Foote, G. B., 1984: A study of hail growth utilizing observed storm conditions. *J. Climate Appl. Meteor.*, **23**, 84–101, doi:10.1175/1520-0450(1984)023<0084:ASOHGU>2.0.CO;2.
- Gilmore, M. S., and L. J. Wicker, 1998: The influence of midtropospheric dryness on supercell morphology and evolution. *Mon.*

- Wea. Rev.*, **126**, 943–958, doi:10.1175/1520-0493(1998)126<0943:TOMDO>2.0.CO;2.
- Hill, G. E., 1974: Factors controlling the size and spacing of cumulus clouds as revealed by numerical experiments. *J. Atmos. Sci.*, **31**, 646–673, doi:10.1175/1520-0469(1974)031<0646:FCTSAS>2.0.CO;2.
- James, R. P., and P. M. Markowski, 2010: A numerical investigation of the effects of dry air aloft on deep convection. *Mon. Wea. Rev.*, **138**, 140–161, doi:10.1175/2009MWR3018.1.
- Klemp, J. B., and R. B. Wilhelmson, 1978: The simulation of three-dimensional convective storm dynamics. *J. Atmos. Sci.*, **35**, 1070–1096, doi:10.1175/1520-0469(1978)035<1070:TSOTDC>2.0.CO;2.
- Knight, C. A., and K. R. Knupp, 1986: Precipitation growth trajectories in a CCOPE storm. *J. Atmos. Sci.*, **43**, 1057–1073, doi:10.1175/1520-0469(1986)043<1057:PGTIAC>2.0.CO;2.
- Lemon, L. R., and C. A. Doswell, 1979: Severe thunderstorm evolution and mesocyclone structure as related to tornado genesis. *Mon. Wea. Rev.*, **107**, 1184–1197, doi:10.1175/1520-0493(1979)107<1184:STEAMS>2.0.CO;2.
- Lilly, D. K., 1962: On the numerical simulation of buoyant convection. *Tellus*, **14**, 148–172, doi:10.1111/j.2153-3490.1962.tb00128.x.
- Loftus, A. M., 2012: A triple-moment bulk hail microphysics scheme to investigate the sensitivities of hail to aerosols. Ph.D. dissertation, Colorado State University, 418 pp. [Available from Dept. of Atmospheric Science, Colorado State University, 200 West Lake Street, Fort Collins, CO 80523.]
- MacGorman, D. R., and D. W. Burgess, 1994: Positive cloud-to-ground lightning in tornadic storms and hailstorms. *Mon. Wea. Rev.*, **122**, 1671–1697, doi:10.1175/1520-0493(1994)122<1671:PCTGLI>2.0.CO;2.
- Markowski, P. M., 2008: A comparison of the midlevel kinematic characteristics of a pair of supercell thunderstorms observed by airborne Doppler radar. *Atmos. Res.*, **88**, 314–322, doi:10.1016/j.atmosres.2007.11.026.
- McCaul, E. W., and C. Cohen, 2002: The impact on simulated storm structure and intensity of variations in the mixed layer and moist layer depths. *Mon. Wea. Rev.*, **130**, 1722–1748, doi:10.1175/1520-0493(2002)130<1722:TIOSSS>2.0.CO;2.
- Meyers, M. P., R. L. Walko, J. Y. Harrington, and W. R. Cotton, 1997: New RAMS cloud microphysics parameterization. Part II: The two-moment scheme. *Atmos. Res.*, **45**, 3–39, doi:10.1016/S0169-8095(97)00018-5.
- Mitchell, D. L., 1996: Use of mass- and area-dimensional power laws for determining precipitation particle terminal velocities. *J. Atmos. Sci.*, **53**, 1710–1723, doi:10.1175/1520-0469(1996)053<1710:UOMAAD>2.0.CO;2.
- Moller, A. R., C. A. Doswell, M. P. Foster, and G. R. Woodall, 1994: The operational recognition of supercell thunderstorm environments and storm structures. *Wea. Forecasting*, **9**, 327–347, doi:10.1175/1520-0434(1994)009<0327:TOROST>2.0.CO;2.
- Nelson, S. P., 1983: The influence of storm flow structure on hail growth. *J. Atmos. Sci.*, **40**, 1965–1983, doi:10.1175/1520-0469(1983)040<1965:TOSFS>2.0.CO;2.
- Parker, M. D., 2012: Impacts of lapse rates on low-level rotation in idealized storms. *J. Atmos. Sci.*, **69**, 538–559, doi:10.1175/JAS-D-11-058.1.
- Rasmussen, E. N., and J. M. Straka, 1998: Variations in supercell morphology. Part I: Observations of the role of upper-level storm-relative flow. *Mon. Wea. Rev.*, **126**, 2406–2421, doi:10.1175/1520-0493(1998)126<2406:VISMPI>2.0.CO;2.
- , —, M. S. Gilmore, and R. Davies-Jones, 2006: A preliminary survey of rear-flank descending reflectivity cores in supercell storms. *Wea. Forecasting*, **21**, 923–938, doi:10.1175/WAF962.1.
- Rasmussen, R. M., and A. J. Heymsfield, 1987: Melting and shedding of graupel and hail. Part III: Investigation of the role of shed drops as hail embryos in the 1 August CCOPE severe storm. *J. Atmos. Sci.*, **44**, 2783–2803, doi:10.1175/1520-0469(1987)044<2783:MASOGA>2.0.CO;2.
- Saleeby, S. M., and W. R. Cotton, 2004: A large-droplet mode and prognostic number concentration of cloud droplets in the Colorado State University Regional Atmospheric Modeling System (RAMS). Part I: Module descriptions and supercell test simulations. *J. Appl. Meteor.*, **43**, 182–195, doi:10.1175/1520-0450(2004)043<0182:ALMAPN>2.0.CO;2.
- , and —, 2008: A binned approach to cloud-droplet riming implemented in a bulk microphysics model. *J. Appl. Meteor. Climatol.*, **47**, 694–703, doi:10.1175/2007JAMC1664.1.
- , and S. C. van den Heever, 2013: Developments in the CSU-RAMS aerosol model: Emissions, nucleation, regeneration, deposition, and radiation. *J. Appl. Meteor. Climatol.*, **52**, 2601–2622, doi:10.1175/JAMC-D-12-0312.1.
- Smagorinsky, J., 1963: General circulation experiments with the primitive equations. I. The basic experiment. *Mon. Wea. Rev.*, **91**, 99–164, doi:10.1175/1520-0493(1963)091<0099:GCEWTP>2.3.CO;2.
- van den Heever, S. C., and W. R. Cotton, 2004: The impact of hail size on simulated supercell storms. *J. Atmos. Sci.*, **61**, 1596–1609, doi:10.1175/1520-0469(2004)061<1596:TIOHSO>2.0.CO;2.
- Walko, R. L., W. R. Cotton, M. P. Meyers, and J. Y. Harrington, 1995: New RAMS cloud microphysics parameterization. Part I: The single-moment scheme. *Atmos. Res.*, **38**, 29–62, doi:10.1016/0169-8095(94)00087-T.
- Weisman, M. L., and J. B. Klemp, 1982: The dependence of numerically simulated convective storms on vertical wind shear and buoyancy. *Mon. Wea. Rev.*, **110**, 504–520, doi:10.1175/1520-0493(1982)110<0504:TDonSC>2.0.CO;2.
- , and —, 1984: The structure and classification of numerically simulated convective storms in directionally varying wind shears. *Mon. Wea. Rev.*, **112**, 2479–2498, doi:10.1175/1520-0493(1984)112<2479:TSACON>2.0.CO;2.
- , and H. B. Bluestein, 1985: Dynamics of numerically simulated LP storms. Preprints, *15th Conf. on Severe Local Storms*, Indianapolis, IN, Amer. Meteor. Soc., 167–171.
- Ziegler, C. L., and E. N. Rasmussen, 1998: The initiation of moist convection at the dryline: Forecasting issues from a case study perspective. *Wea. Forecasting*, **13**, 1106–1131, doi:10.1175/1520-0434(1998)013<1106:TOMCA>2.0.CO;2.